ORIGINAL RESEARCH ARTICLE

A Comparative Study on Microstructure, Mechanical Properties and Corrosion Resistance of M390 and 304 with Different Welding Methods

Zishen Liu, Lixue Qiao, Rui Cao, Hao Dong, Caiqin Wang, Hongyan Che, Tiejun Wang, and Yinjie Yan

Tungsten argon arc welding (TIG), cold metal transfer (CMT) welding and flash butt welding (FBW) are used to join M390 and 304. The mechanical properties of M390 and 304 welded joints with different welding methods were compared by tensile and microhardness experiments. The microstructure evolution and phase changes of TIG, CMT and FBW welded joints were compared and analyzed by scanning electron microscope (SEM) and x-ray diffraction. The grain size of weld metal (WM) and M390 heat-affected zone of three types of welded joints were measured by Image J software. Corrosion resistance of three types of weld joints was characterized by electrochemical corrosion tests, and the microstructure of post-corrosion test specimens was characterized by SEM and EDS. The results show that three types of welded joints without cracks and voids can be obtained between dissimilar metals M390 and 304. The microstructure of TIG weld metal is composed of martensite and the carbides M_7C_3 and $M_{23}C_6$ due to higher heat input during TIG welding processes. Because extensive C, Cr and Ni element diffusion occurs during FBW welding due to low heat input, the microstructure of the weld metal is composed of martensite and austenite matrix and carbides of M_7C_3 and $M_{23}C_6$. The filling of nickel-based alloys during CMT welding processes make the microstructure include austenite and (Al, Ni, Ti) carbide. The tensile strength and elongation of CMT welded joint can reach 501 MPa and 21.8%, the corrosion current density is 4 mA cm^{-2}, and the corrosion voltage is − 21 mV, which is the best mechanical properties among the three types of welded joints. The welded joints with the three welding methods are all fractured at WM position.

1. Introduction

A high carbon, high-chromium martensitic stainless steel M390 prepared by hot isostatic pressing (HIP) and subsequent heat treatment has advantages of high hardness, high strength, excellent corrosion resistance and good wear resistance. It is mainly used in advanced knife materials, mold steel, aerospace and other fields. In most cases, M390 needs to be joined with other structural parts to prepare a complex structure. Therefore, it is necessary to investigate the weldability of M390. 304 austenitic stainless steel is the most widely used stainless steel in industrial production and daily life. The welding of M390 and 304 becomes the most important problem to be solved M390 application in various fields. For the welding of high

carbon martensitic stainless steel, martensitic microstructure with coarse grains and hydrogen-induced cracks are easily produced at the weld metal and the side of the high carbon martensitic heat-affected zone (Ref 1). 304 shows good corrosion resistance and weldability when welding with other dissimilar metals (Ref 2-6). Therefore, it is difficult to join M390 and 304 because of hard and brittle martensitic microstructure in M390 heat-affected zone and weld metal. Many scholars use a variety of fusion welding methods, such as laser welding, TIG welding, arc welding and other methods to welding martensitic stainless steel and austenitic stainless steel (Ref 7-11). TIG welding and more advanced A-TIG and K-TIG are widely used in the joining of thin plate joints (Ref 12, 13). CMT welded M390 and 304 stainless steel joints are widely used in the production of advanced tools (Ref 14). The results show that for welded joint obtained by traditional fusion welding method, due to excessive heat input martensitic microstructure with coarse grains appears on the side of the martensitic heat-affected zone and weld metal. Some scholars join martensitic stainless steel and austenitic stainless steel by solid-state welding, such as resistance butt welding, flash butt welding and friction welding (Ref 1, 15-18). The results show that fine equiaxed grains can mainly be formed in the heat-affected zone on the martensite side, which is smaller than that of traditional fusion welding, so the mechanical properties are improved.

The predecessors employed nickel-based alloys as filler wire to prevent carbon components from diffusing into the weld metal (Ref 19-21). Sirohi et al. (Ref 22) successfully joined P91

Zishen Liu, Lixue Qiao, Rui Cao, and **Yinjie Yan**, State Key Laboratory of Advanced Processing and Recycling of Non-ferrous Metal, School of Materials Science and Engineering, Lanzhou University of Technology, Lanzhou 730050, China; and **Hao Dong, Caiqin Wang, Hongyan Che,** and **Tiejun Wang**, Advanced Technology & Materials Limited Company, China Iron & Steel Research Institute Group, Beijing 100081, China. Contact e-mail: caorui@lut.edu.cn.

and 304 by nickel-based 625 alloy wire and found that nickel-based 625 alloy has a strong inhibitory effect on carbon migration in P91/304 welded joints. Pratishtha et al. (Ref 23) joined dissimilar metals between martensitic and austenitic steels by filled nickel-based welding wire ErNiCrMo-3 and unfilled welding wire. A large amount of hard and brittle martensitic microstructure is formed in weld metal for the joint without filler wire, which leads to lower tensile strength and impact toughness. The addition of ErNiCrMo-3 nickel-based welding wire changes the ratio of Cr and Ni elements in weld metal, and the microstructure in weld metal from hard and brittle martensite to austenite. Anup et al. (Ref 24) welded P91 and 316L with nickel-based 800 and nickel-based 600 as filler wire. The addition of various nickel-based wires affects the various microstructure of weld metal and the various mechanical properties of the welded joint. Therefore, filled nickel-based alloys not only improved the toughness of the welded joint and suppressed the diffusion of carbon elements.

In welded joints, the relationship between microstructure changes and mechanical properties has also been studied by predecessors. Sabzi et al. (Ref 25, 26) studied the effect of pulsed current on dissimilar welded joint of AISI 316L-AISI 310S stainless steels. Pulsed mode changed the morphology of the grains from the elongated columnar to coaxial one and substantially reduced the grain size to improve the hardness and fracture toughness of the joint. The same phenomenon was also observed in the joints of 316L after electromagnetic stirring and pulse current, which also improved the mechanical properties of the joints (Ref 27, 28). In terms of microstructure, Mousavi Anijdan et al. (Ref 29) obtained high strength and hardness martensite in dissimilar joint of dual phase steel DP600 and AISI 304 stainless steel by changing the process parameters and optimized the shear tensile strength.

Considering above, by comparing mechanical properties, corrosion resistance and microstructure characteristics of M390 and 304 welded joints with traditional fusion welding (TIG), improved gas shielded welding (CMT) and Flash butt welding (FBW), appropriate welding method and welding process are recommended.

2. Experimental Procedure

2.1 Materials

M390 powder metallurgy high-carbon martensitic stainless steel was prepared by Advanced Technology & Materials Limited Company. Commercial 304 austenitic stainless steel was used in this paper. The chemical composition of 304 stainless steel follows the standard ASTM A313/A313M-2018. Table 1 shows corresponding chemical composition of M390 and 304. Table 2 shows physical properties of M390 and 304.

Large differences appear in C and Ni elements content, physical properties (such as thermal expansion coefficient) and mechanical properties (such as strength, hardness and elongation).

2.2 Welding process

(1) Tungsten argon arc welding (TIG) processM390 and 304 steels are joined without wire filler by an automatic TIG welding machine with argon gas as a shielding gas and gas flow rate of 15 L/min. Before welding, oxide film on the specimen's surface was removed and cleaned with acetone. The welding diagram is shown in Fig. 1(a), and the optimized TIG welding process parameters are shown in Table 3.

(2) Cold metal transition welding (CMT) processM390 and 304 steels were butt welded by cold metal transfer welding (CMT) machine with argon gas as shielding gas and gas flow rate of 15L/min. In order to inhibit the diffusion of C and Cr elements and improve the toughness of weld metal, ERNi-1 welding wire is selected as the filler metal in CMT welding. The wire extension of 2mm was set. The angle of the groove between two plates is set as 60°. The torch is inclined at 45°. Before welding, the oxide film of two plates was treated and cleaned with acetone. The welding schematic diagram is shown in Fig. 1(b). The optimized CMT welding process parameters are shown in Table 3.

(3) Flash butt welding (FBW) welding processThe two butt welding surfaces of M390 and 304 steels were treated and polished before welding to keep them smooth and flat. CO_2, CO and metal vapors released at the butt welding surface during flash butt welding form a self-protection effect at the butt welding position. No external gas protection is required during welding processes. After welding, the extruded residue at the weld metal needs to be cleaned. The welding schematic diagram is shown in Fig. 1(c), and the optimized flash butt welding process parameters are shown in Table 4.

2.3 Microscopic Analysis

The metallurgical specimens were cut and prepared from three types of welded joints to compare the difference of microstructure using SEM and EDS. Before SEM and EDS experiments, the metallurgical specimens of the three types of welded joints needed to be polished, cleaned with acetone and then etched by a mixed solution of $FeCl_3$ and hydrochloric acid ($FeCl_3/HCl/H_2O = 1:3:3$). The grain size of weld metal and M390 heat-affected zone in three welded joints was measured by Image J.

Table 1 Chemical composition of M390 and 304 steels (in wt.%)

Steels	C	Cr	Mn + Mo + Si + V	Ni	W	Al	Ti	Cu + P + S	Fe
M390	1.97	19.7	5.9	…	0.63	…	…	…	BAL
304	0.07	19	3	11	…	…	…	…	BAL
ERNi-1	0.03	…	0.77	94.421	…	1.17	2.74	0.119	0.75

Table 2 Mechanical properties and physical properties of M390 and 304 steels

Material	σ_b (MPa)	δ (%)	Hardness (HV)	ρ (kg/dm^2)	α (10^{-6}*K^{-1})
M390	≥ 900	5.54	300-400	7.53	10.4
304	≥ 520	18	180-200	7.93	17.2

σ_b tensile strength, δ elongation, ρ density, α linear expansion coefficient.
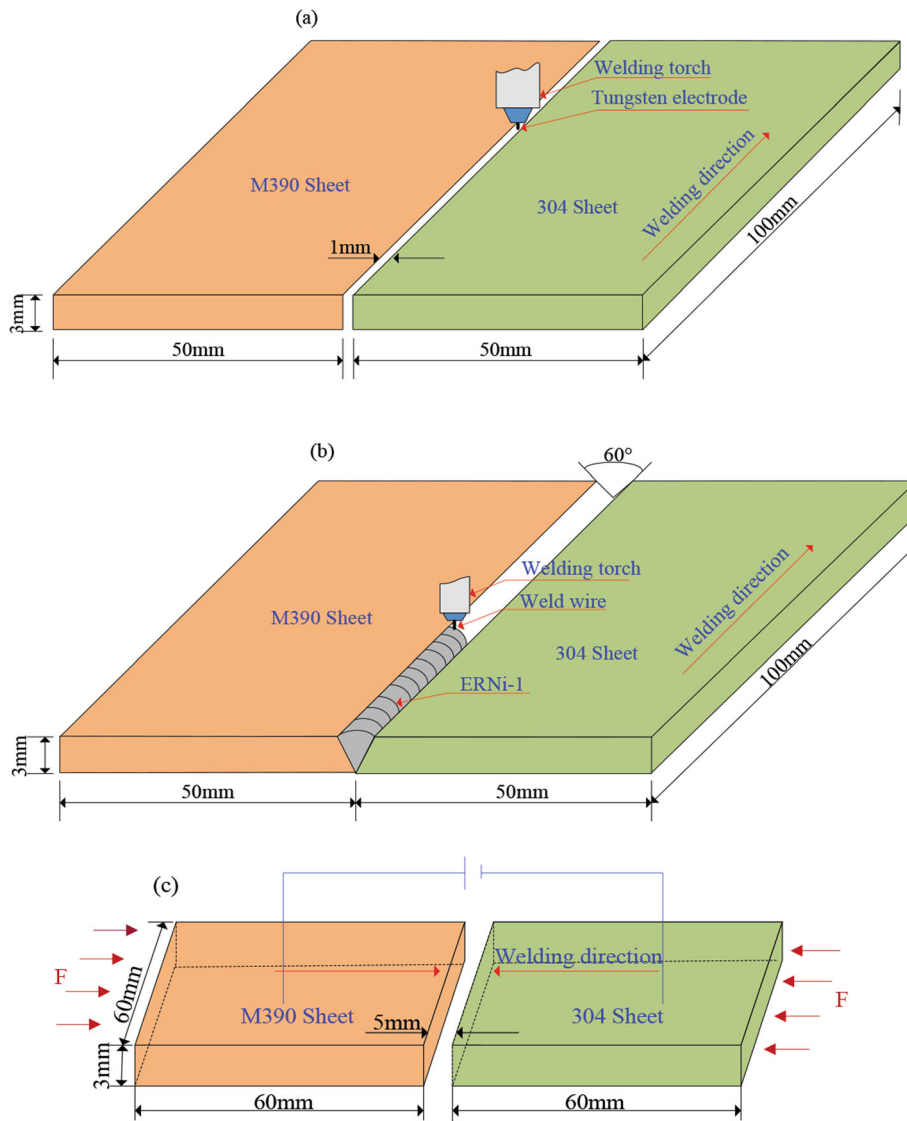
Fig. 1 Schematic diagram of CMT, TIG and FBW (a) TIG, (b) CMT, (c) FBW

Table 3 Optimized TIG welding parameters

Welding methods	Welding speed, mm/s	Wire feeding speed, m/min	Welding current, A	Welding voltage, V
TIG	2.3	…	120	16
CMT	4.5	9	110	18.1

Table 4 Optimized FBW welding parameters

Flash current, A	Flash time, s	Upsetting current, A	Upsetting time, s	Tempering current, A	Tempering time, s
732	133	530	25	554	0

2.4 Characterization of Tensile Strength and Hardness

Tensile specimens were prepared from three types of weld joints with optimized welding parameters. Three tensile specimens are prepared for each welded joint. Before tensile test, all the outer surfaces of tensile specimen are smoothly polished by sandpaper to avoid defects because higher stress concentration produced at the surface defects affects tensile performance. Tensile strength was measured by IN-STRON8801. Microhardness was measured from M390 base metal through weld metal to 304 base metal by Wilson VH1102 hardness tester.

2.5 Measurement of the Corrosion Resistance

Corrosion resistance test is based on ISO 17475:2005. Corrosion resistance of three welded joints was revealed by electrochemical experiments. The size of prepared specimen was 10 mm × 10 mm × 3 mm. After polishing, it was corroded with 3.5% NaCl solution. Corrosion current and corrosion voltage were tested by VersaSTAT 3F electrochemical workstation, and polarization curve was obtained. The microstructure of the three welded joints after corrosion was observed by SEM and EDS.

3. Results

3.1 Weld Appearance of TIG, CMT and FBW Welded Joints

The weld appearance was evaluated according to ISO 15614-1 standard. Figure 2 shows the weld appearance of TIG, CMT and FBW weld joints. The weld metal with a beautiful appearance and without defects such as cracks and holes can be obtained. In Fig. 2(e), the local straight FBW weld metal is partially extruded to the specimens' surface. Figure 3 shows the cross-sectional morphology of the M390/304 welded joints. Three types of welded joints are all composed of M390 base metal (M390BM), M390 fine grain heat-affected zone (FGHAZ), M390 coarse grain heat-affected zone (CGHAZ), weld metal (WM), 304 heat-affected zone (304HAZ), 304 base metal (304BM).

3.2 Comparison of Microstructure in TIG, CMT and FBW Welded Joints

Figure 4 compares the microstructure of M390 base metal and M390 heat-affected zone in three types of welded joints. The results show that long-strip carbides are distributed on the grain boundaries of TIG and CMT-CGHAZ, while block carbides are distributed on the grain boundaries of FBW-CGHAZ. Different heat inputs are obtained in three welded joints due to different welding methods and different corresponding welding parameters. Figure 5 presents the microstructure of three welded metals. From Fig. 5, the morphologies of three types of weld metals are quite different. In Fig. 5(a), TIG

WM is composed of martensite matrix with long columnar crystals and a large number of carbide particles distributed on the grain boundaries. In Fig. 5(b), CMT WM is composed of austenite matrix with coarse grain size and carbides, most carbides exist in irregular morphology, and a small amount of carbides are distributed on the grain boundaries. In Fig. 5(c), FBW WM is also composed of equiaxed grain martensite matrix and a small amount of carbides distributed on the grain boundaries. Table 5 shows corresponding point scanning results in Fig. 4(f) and 5(b). The results of point 1 and point 2 in Table 5 can further confirm that carbides on M390 side are (Cr, V) carbides. However, the results of point 3 and 4 in Table 5 show that carbides in CMT WM are (Al, Ni, Ti) carbides, which is further proved in Fig. 6(b). Al and Ti elements of (Al, Ni, Ti) carbides in CMT WM come from the filler wire (ERNi-1), as shown in Table 1. The carbide development patterns in M390 base metal, FGHAZ and CGHAZ are all the same in the three welded joints. The carbide morphology changes from granular to elongated shape from M390 base metal to coarse-grained zone. The various heat inputs were used for three welding procedures, which induces the difference of austenitization in the heat-affected zone during the welding process and the difference of carbide precipitation after cooling. The heat input of the TIG welded joint is undoubtedly the largest, resulting in the presence of long-striped carbides in the coarse-grained zone. However, the heat input of the FBW welded joint is the lowest, which induces the formation of granular carbides in the coarse-grained zone.

Figure 6 shows XRD analysis results of different regions for three types of welded joints. Different regions include M390 BM, M390 FGHAZ, M390 CGHAZ, 304 HAZ and 304 BM. However, the phase composition of WM in three types of welded joints has significant changes. M390 BM is composed of martensite, a small amount of retained austenite, $M_{23}C_6$ and M_7C_3. M390 FGHAZ and M390 CGHAZ are composed of martensite, $M_{23}C_6$ and M_7C_3. Proportion of $M_{23}C_6$ and M_7C_3 in two regions is changed. 304 HAZ is composed of martensite, austenite, $M_{23}C_6$ and M_7C_3. 304 BM is composed of austenite and $M_{23}C_6$. The five phases in XRD analysis are austenite, martensite, $M_{23}C_6$, M_7C_3 and $Al_{0.5}CNi_3Ti_{0.5}$, and their card numbers are 04-002-3692, 04-002-1061, 00-035-0783, 00-036-1482 and 00-019-0035, respectively. The microstructure of TIG weld metal is composed of martensite and the carbides M_7C_3 and $M_{23}C_6$ due to the large heat input during TIG welding. Low heat input and extensive C, Cr and Ni element diffusion occur during FBW welding, which induces the microstructure of the weld metal matrix is martensite and austenite except for carbides of M_7C_3 and $M_{23}C_6$. The filling of nickel-based alloys during CMT welding makes the appearance of austenite and (Al, Ni, Ti) carbide.

Figure 7 shows statistical results about grain size of M390 HAZ and WM for three welded joints. In Fig. 7(a), TIG-FGHAZ has the largest grain size. In Fig. 7(b), TIG-CGHAZ has the largest grain size. In Fig. 7(c), CMT WM has the largest grain size. The average grain size of TIG-CGHAZ, FGHAZ,
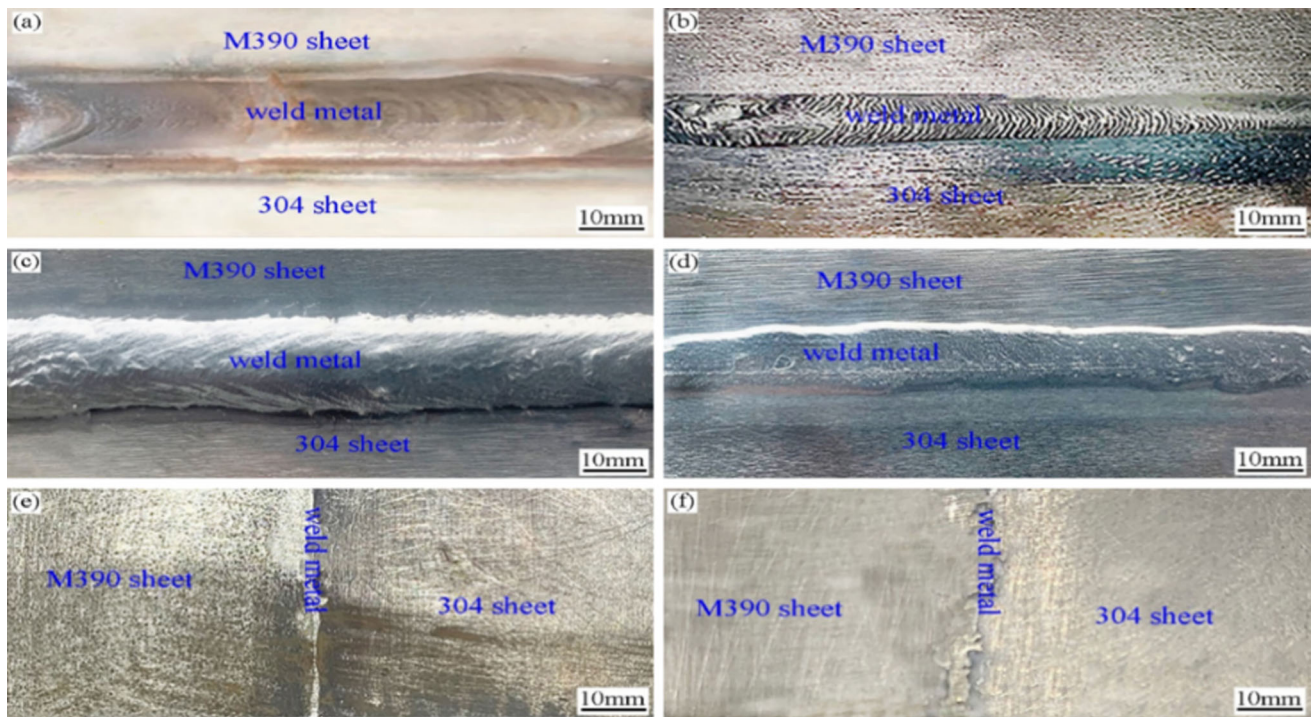
Fig. 2 Weld appearance of M390/304 welded joints (a) TIG-front side, (b) TIG-back side, (c) CMT-front side, (d) CMT-back side, (e) FBW-front side, (f) FBW-back side
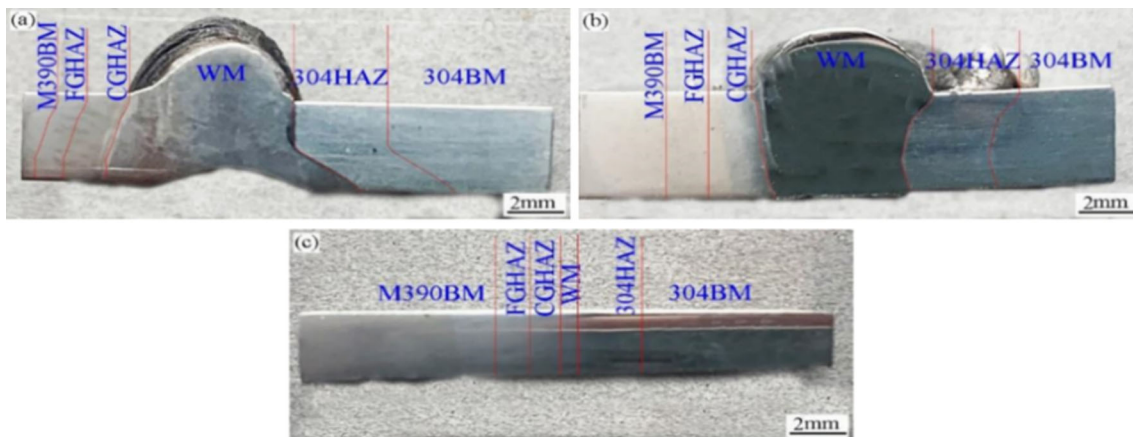

Fig. 3 Cross section of M390/304 welded joints (a) TIG, (b) CMT, (c) FBW

WM is 11.6, 8.25, 17.96 μm. The average grain sizes of CMT-CGHAZ, FGHAZ, WM are 5.32, 3.22, 24.78 μm. The average grain sizes of FBW-CGHAZ, FGHAZ and WM are 5.02, 3.17 and 7.81 μm, respectively. There are more grain boundaries when grain size decreases. At the grain boundary, the crystal arrangement is very irregular, and the crystal planes connected to one another, enhancing the bonding force between metals.

In conclusion, through analysis of microscopic morphology, phase composition, carbide distribution and grain size statistics in TIG, CMT and FBW welded joints, CMT and FBW welding methods have their own advantages. Because nickel-based wire is filled in CMT, austenitic phase is formed in CMT WM, resulting in higher toughness. FBW WM and heat-affected zone have finer grain size due to low heat input for FBW.

3.3 Hardness Analysis of TIG, CMT and FBW Weld Joints

Generally, distribution of hardness in the weld metal depends on mismatch rate between weld metal and base metal (Ref 30). When filler wire with a higher mismatch rate is used in weld metal, hardness of the weld metal is higher than that of base metal (Ref 31-33). On the contrary, when filler wire with lower mismatch ratio is used in the weld metal, the hardness of the weld metal is lower than that of base metal. Figure 8 shows the hardness distribution of three types of weld joints. In Fig. 8(a), the hardness of M390 HAZ, WM and 304 HAZ in TIG welded joint has little change. In Fig. 8(b), for CMT welded joint, the hardness gradually increases from M390 BM to M390 CGHAZ, but a large hardness difference is appeared between M390 CGHAZ and WM. The hardness has a tendency
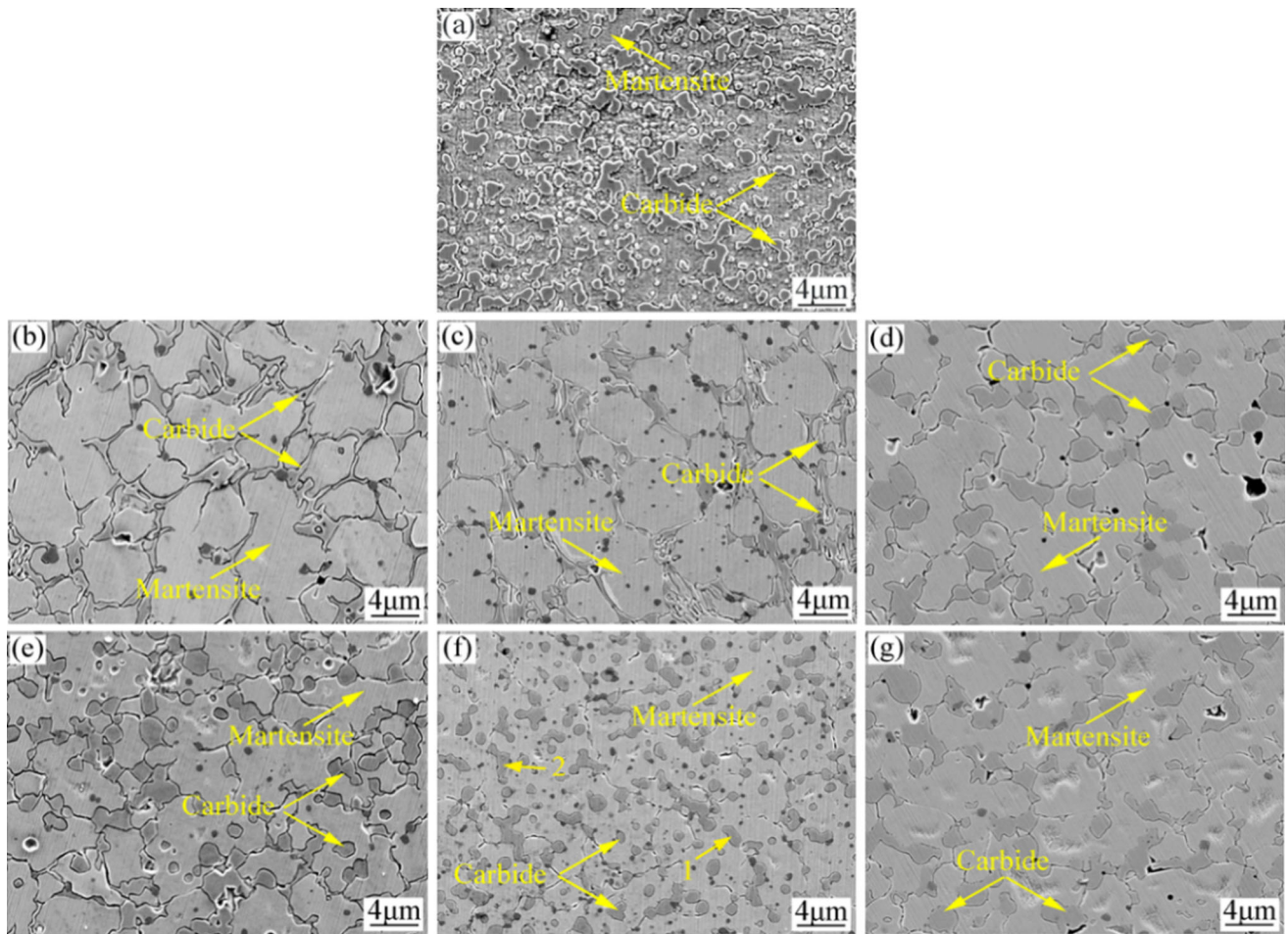
Fig. 4 Microstructure of M390 base metal and M390 heat-affected zone for three welded joints (a) M390BM, (b) TIG-CGHAZ, (c) CMT-CGHAZ, (d) FBW-CGHAZ, (e) TIG-FGHAZ, (f) CMT-FGHAZ, (g) FBW-FGHAZ
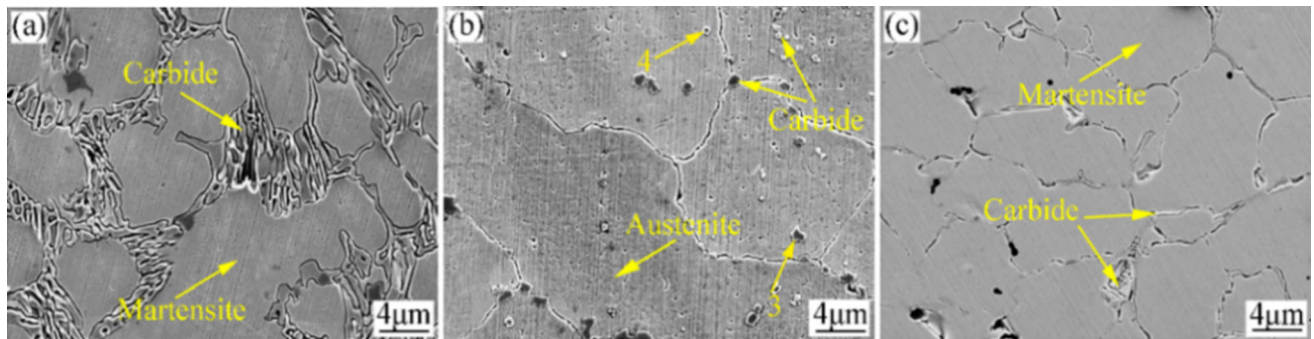

Fig. 5 Microstructure of the weld metal (a) TIG, (b) CMT, (c) FBW

Table 5 Point scanning analysis of the welded joints in Fig. 5e and 6b (in at.%)

Points	Fe	C	Cr	V	Mo	Ni	Ti	Al
1	21.1	44	29.2	5.3	0.3	…	…	…
2	19.6	44.4	30	5.7	0.3	…	…	…
3	…	31.8	…	…	…	28.4	39.6	0.2
4	…	52.6	…	…	…	47.1	0.2	0.1

to increase firstly and then decrease at 304 HAZ. In Fig. 8(c), the hardness gradually increases from M390 BM to M390 CGHAZ. From M390 CGHAZ, WM, 304 HAZ to 304 BM, the hardness shows a decreasing trend.

3.4 Comparison of Tensile Properties and Fracture Analysis of TIG, CMT and FBW Welded Joints

Tensile results of TIG, CMT and FBW welded joints are shown in Fig. 9, and the yield strength, tensile strength and
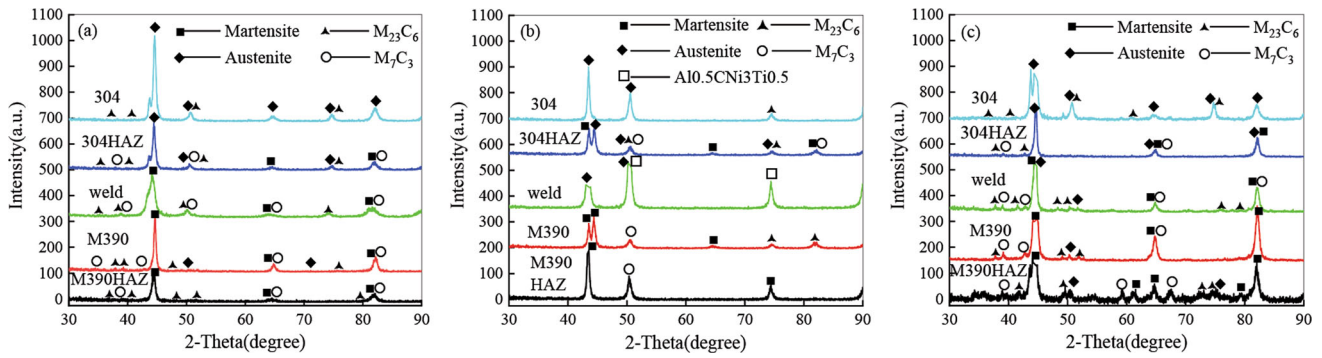
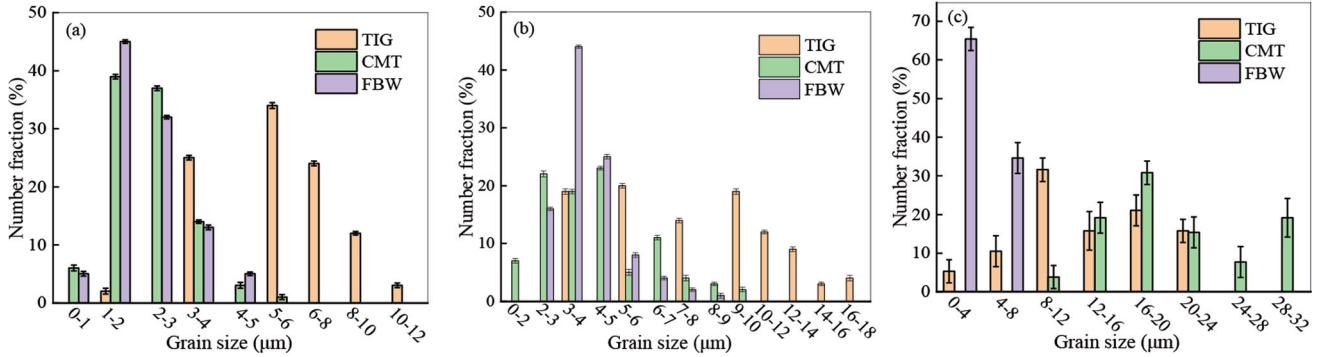**Fig. 6** XRD results of M390/304 welded joints and base metals (a) TIG, (b) CMT, (c) FBW

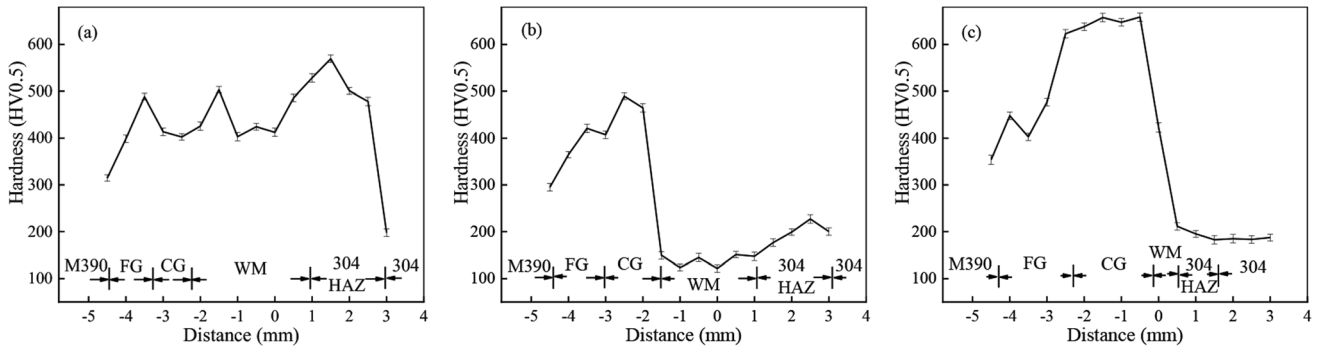**Fig. 7** Grain sizes of M390/304 welded joints (a) FGHAZ, (b) CGHAZ, (c) WM

Fig. 8 Hardness distribution of M390/304 welded joints (a) TIG, (b) CMT, (c) FBW

elongation of the three welded joints are measured. Since TIG, CMT and FBW welded joints have no obvious yield platform, the stress $\sigma_{0.2}$ is used as the yield strength. As shown in the figure, the yield strength of TIG, CMT and FBW welded joints is 257, 223 and 328 MPa, respectively, indicating that the CMT welded joint has the lowest yield strength and the FBW welded joint has the highest yield strength. The tensile strength of CMT welded joint reaches 501 MPa. Tensile strength of CMT welded joint reaches 57 and 62% that of M390 BM and 304 BM, respectively. CMT welded joint can reach the highest elongation of 21.8%, which is 360% of M390 BM elongation and 34% of 304 BM elongation. It shows that the elongation of the CMT welded joint is already higher than that of M390 BM. The tensile strength and elongation of TIG welded joint only reach 266 MPa and 0.045%, respectively. Tensile strength of TIG welded joint only reaches 30 and 33% that of M390 BM and 304 BM, respectively. So, the mechanical properties of TIG

welded joint are very poor. The tensile strength of FBW welded joint can reach 480 MPa. Tensile strength of FBW welded joint reaches 54 and 59% that of M390 BM and 304 BM, respectively. Its elongation is similar to that of M390 BM. Combined in Fig. 10, among the three types of welded joints, the tensile strength and elongation of CMT are best, but the yield strength is the lowest, followed by the better mechanical properties of FBW.

Figure 10 shows fracture surfaces of TIG, CMT, FBW welded joints. Cleavage fracture dominates fracture surfaces of TIG, and brittle fracture dominates fracture surfaces of FBW welded joints. The occurrence of brittle fracture is related to the material itself, which may be caused by the presence of carbides or other impurities. Plastic deformation is rarely produced during fracture (Ref 34, 35). Ductile fracture dominates fracture surface of CMT. As a soft phase, the fracture mechanism of austenite is generally the nucleation,
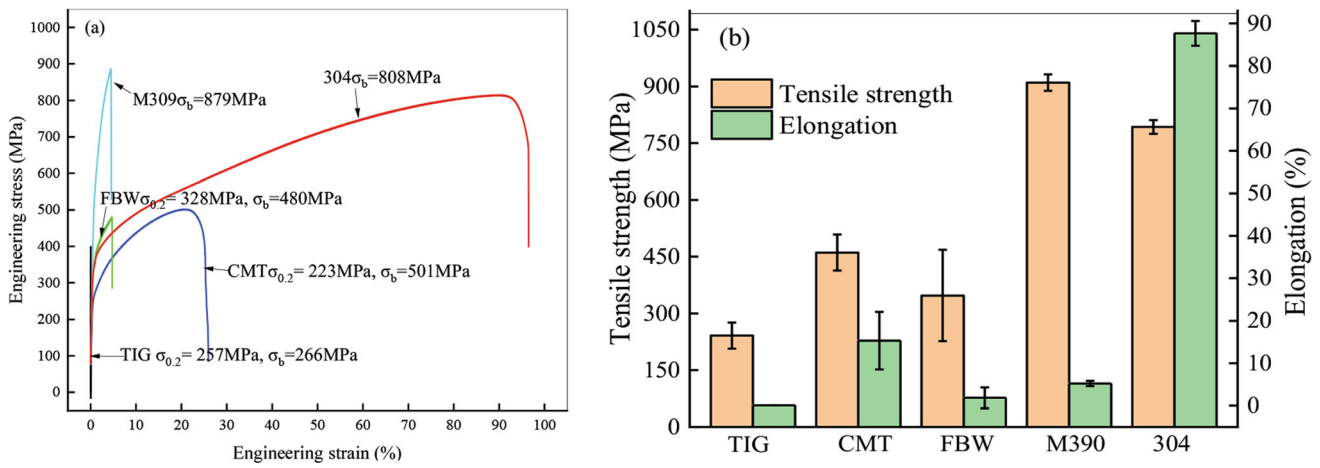
Fig. 9 Tensile properties of M390/304 welded joints and base metals (a) engineering stress–engineering strain curves, (b) tensile strength and elongation
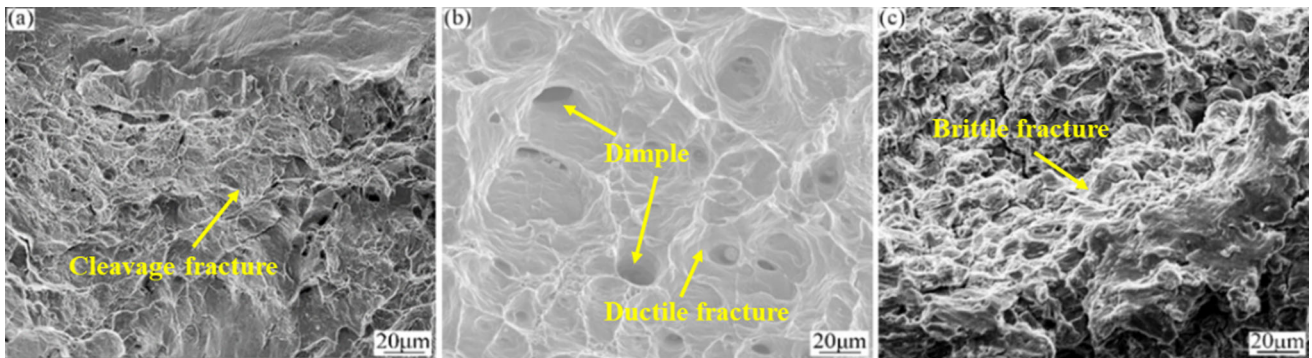

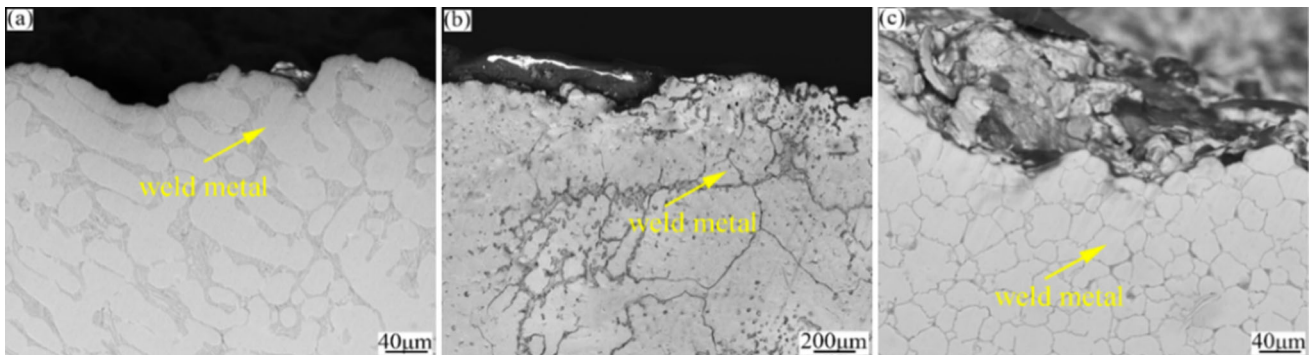**Fig. 10** Tensile fracture surfaces of M390/304 welded joints (a) TIG, (b) CMT, (c) FBW

Fig. 11 Fracture position of M390/304 welded joints (a) TIG, (b) CMT, (c) FBW

growth and coalescence of pores, that is, cone and cup fracture (Ref 36, 37). It means that fracture surfaces of three welded joints have greatly changed due to the using of various welding methods and various welding materials. Various welding methods and various welding materials cause differences in microstructure of the WM, which is the main reason for the formation of different fracture features.

Figure 11 shows microstructures at the fracture locations of TIG, CMT and FBW welded joints. TIG joint is fractured at the weld metal which the grains exhibit a dendritic morphology in Fig. 11(a). CMT joint is fractured at the nickel weld metal with

the irregular morphology grains, which is consistent with Fig. 11(b). FBW joint is also fractured at the weld metal with a regular equiaxed grain morphology, which are the same as WM morphology in Fig. 11(c).

3.5 Corrosion Resistance of TIG, CMT and FBW Weld Joints

Dynamic electrode potential curves of TIG, CMT and FBW welded joints in the same concentration of NaCl solution are shown in Fig. 12. The corrosion potential of TIG, CMT and FBW welded joints reaches − 45, − 21 and − 48 mV,

respectively. The corrosion current density of TIG, CMT and FBW welded joints reaches 2.3, 4 and 8.7 mA cm^{-2}, respectively. According to corrosion potential, corrosion current density and polarization curve, it can be seen that CMT welded joint has best corrosion resistance. FBW welded joint has poor corrosion resistance. The main reason for good corrosion resistance of CM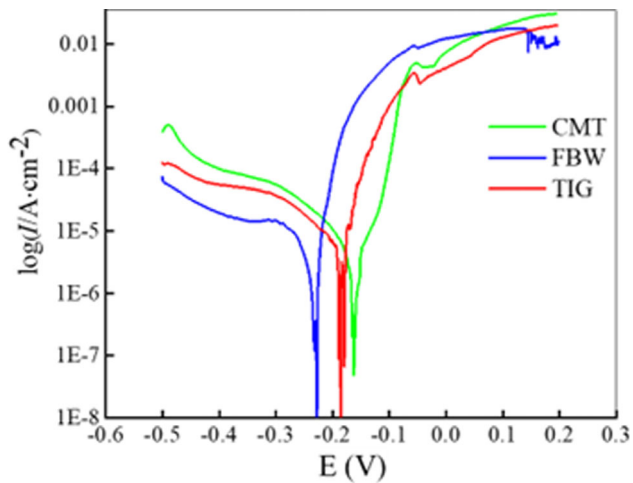T welded joint is that WM is filled with nickel-based alloys. Figure 13 shows the SEM and EDS observation results after electrochemical corrosion. It can be observed from the SEM image that pitting corrosion pits are the main electrochemical corrosion forms in the three joints. Among them, the pitting corrosion pit of the CMT specimen is the smallest, the pitting corrosion pit of the TIG specimen is larger and the distribution is more uniform, and the pitting corrosion pit in the FBW specimen is the largest and the size distribution is not uniform. According to EDS analysis, due to the addition of nickel-based alloy welding wire to the CMT specimen, the weld metal is rich in a large number of evenly distributed Ni elements, and no segregation of elements was observed near the pitting corrosion pit. Compared with the uniform distribution of elements in TIG joints, the elements of FBW have obvious segregation, and obvious Cr depletion can be observed at the location of pitting corrosion pit.

Fig. 12 Corrosion resistance analysis of the M390/304 welded joints

4. Discussion

4.1 Mechanisms of Three Welded Joints Fractured at the Weld Metal

Fracture surfaces of three types of welded joints show different morphologies, as shown in Fig. 10, while the fracture positions of three types of weld joints are all located at WM, as shown in Fig. 11. The heat-affected zone and WM of dissimilar metals welded joints are two weaker regions (Ref 38-40). The
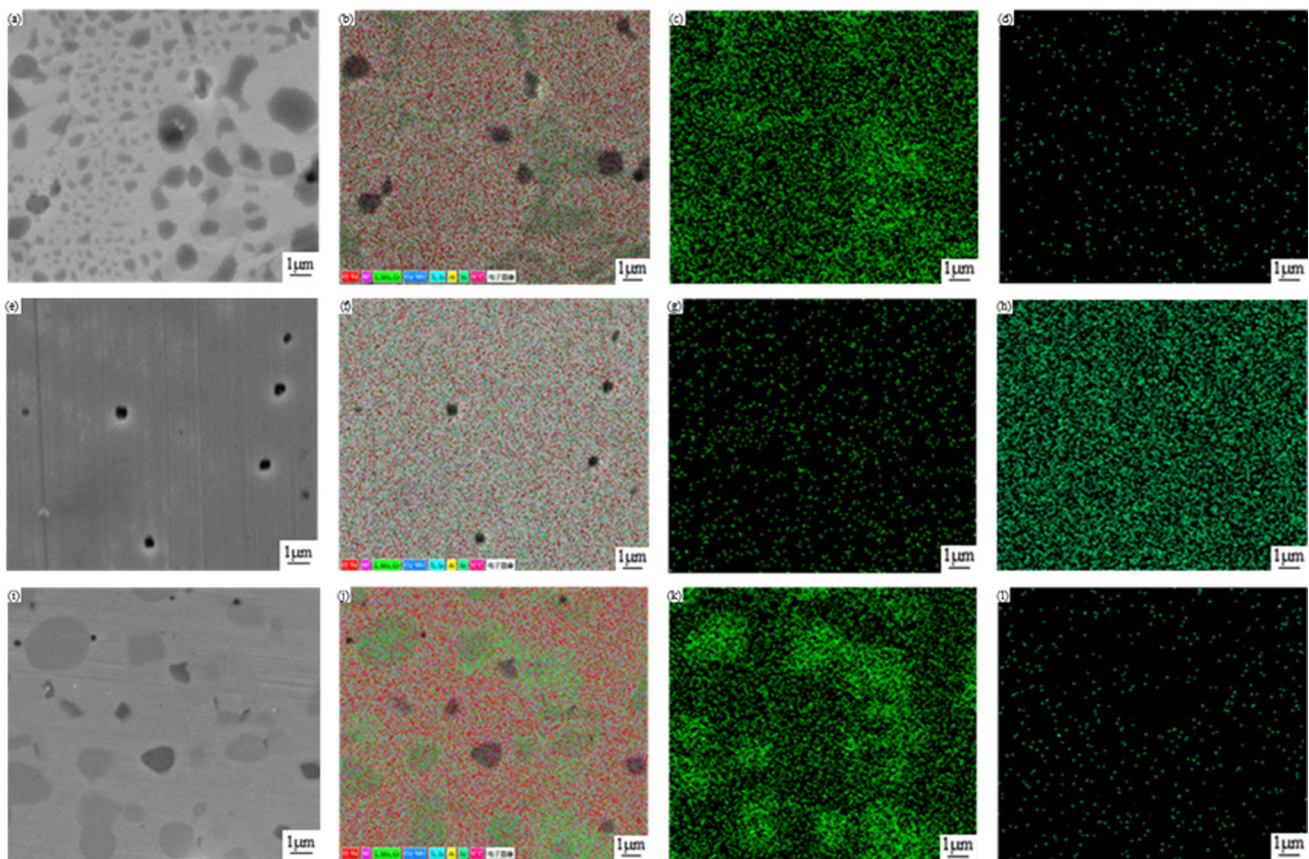

Fig. 13 Microstructure and element distribution of the weld metals in three welded joints after corrosion test (a) TIG-SEM, (b) TIG-EDS, (c) TIG-Cr Kα1, (d) TIG-Ni Kα1, (e) CMT-SEM, (f) CMT-EDS, (g) CMT-Cr Kα1, (h) CMT-Ni Kα1, (i) FBW-SEM, (j) FBW-EDS, (k) FBW-Cr Kα1, (l) FBW-Ni Kα1

brittle martensite microstructure has a high tendency to crack initiation in coarse-grained heat-affected zone and WM (Ref 41-43). According to the grain size of Fig. 7 and XRD analysis results of each area in Fig. 6, the welded joint of M390 high carbon martensite and 304 austenitic stainless steel is easily fractured in WM due to the formation of martensite with coarse grains. For M390 and 304 TIG welded joint, brittle martensite is produced in WM and M390 CGHAZ. Moreover, coarse grain size in WM and composition segregation during WM solidification process (Ref 44) lead to the formation of the solidification cracks (Ref 45) and other defects, which induces the welded joint finally fracture in WM. Zhang et al. (Ref 46) investigated welding of 10% Cr martensitic steel and 617B nickel-based alloy filled with nickel-based metal, and it shows that the failure between martensite and nickel-based alloy is related to factors such as corrosion under oxidation, interfacial precipitates and thermal expansion coefficient mismatchment. The CMT welded joint of M390 and 304 is fractured at WM position. From Fig. 10(b), the fracture is caused by the coarsest grain in CMT WM which is much larger than that of M390 CGHAZ. FBW welded joint is also fractured in WM. The number of carbides distributed on WM grain boundaries of FBW welded joint in Fig. 4 and 5 is far less than that M390 CGHAZ. The pinning effect of carbides in WM is significantly weakened. In FBW process, due to large difference in chemical composition on both sides of M390 and 304, a chemical potential can be formed (Ref 47), which promote diffusion of C, Cr, Ni and other elements in WM, resulting in uneven chemical composition in WM, finally causing the specimen fracture at WM.

4.2 Reason of Hardness Difference for Three Welded Joints

From Fig. 8, for three welding methods, microhardness of M390 and 304 welded joint is also different. Huang et al. (Ref 48) investigated the diffusion of carbon element in dissimilar metals $Cr_5Mo/Cr_{21}Ni_{12}$ welded joint and showed that a decarburized layer was formed on the side of pearlitic steel (Cr_5Mo), which reduces tensile strength and creep resistance, and a recarburized layer is formed on the side of austenitic steel ($Cr_{21}Ni_{12}$), so hardness in this area increases. Due to high heat input of M390 and 304 TIG welded joint, a large amount of martensite is formed in WM and the heat-affected zone on both sides, resulting in little change hardness in M390 HAZ, WM and 304 HAZ. However, the peak of hardness appears in 304 HAZ, mainly due to the formation of a carburized layer in this area. A huge hardness difference between M390 CGHAZ and WM is appeared for CMT welded joint, which is directly related to nickel-based alloy filled in WM. The solubility of carbon in nickel-based alloys is very low, which can effectively hinder the diffusion of carbon elements (Ref 19, 44, 45, 49), avoid the formation of dangerous areas such as decarburization and recarburization layers and the lower hardness of nickel-based alloys, which leads to the formation of huge hardness differences. The hardness between CMT WM and 304 BM first increases and then decreases because martensite microstructure is formed in 304 HAZ. Gittos (Ref 50) pointed out that after carbon element migrates to WM, only a small amount of carbon dissolves into the matrix, and most of it combines with Cr to form carbides, and the diffusion of C and Cr elements increases M_s of CGHAZ, resulting in a further increase of martensite microstructure. The hardness of FBW welded joint gradually increases between M390 BM and M390 CGHAZ, which is affected by heat input, and the hardness of WM shows a

gradually decreasing trend, mainly due to the diffusion of C and Cr elements in WM.

4.3 Reason of Strength and Elongation Difference for three welded joints

Figure 9 shows that mechanical properties of M390 and 304 welded joints with various welding methods and various welding variables. Firstly, a strong correlation between the yield strength and the grain size is found. The relationship between the yield strength and inverse square root of grain size is drawn in Fig. 14 and has a good linear relationship, which is the so-called Hall–Petch equation (Ref 57, 58):

$$\sigma = \sigma_0 + kD^{-0.5} \tag{Eq 1}$$

In the formula, σ_0 is the lattice friction stress required to move a single dislocation, k is the Hall–Petch coefficient, and D is the average grain size. The H-P coefficient in this study is 20.54 MPa mm$^{0.5}$. In the study of Tan et al. (Ref 59), 600 MPa μm$^{0.5}$ was used as the reference value of H-P coefficient of martensitic stainless steel. Park (Ref 60) and Astafurov (Ref 61) obtained the H-P coefficients of austenitic stainless steels, which were 6.7-37.0 MPa mm$^{0.5}$ and 4.1-22.0 MPa mm$^{0.5}$, respectively. Therefore, the H-P coefficient in this study is within the reported range. Secondly, it was found that the tensile strength and elongation of the welded joint of CMT filled nickel-based alloy were the best. On the one hand, nickel-based metal can effectively hinder carbon migration and avoid the formation of decarburization and carburization layers and other dangerous areas (Ref 19). Nickel-based filler metal has high toughness, which can reduce the residual stress formed by welding and reduce the formation of welded cracks (Ref 51, 52). On the other hand, fine heat-affected zone grains are obtained in Fig. 7 because heat input of CMT as an improved MIG welding is much lower than that of traditional fusion welding (Ref 19, 53). Secondly, tensile strength of FBW welded joint has no much different from that of CMT welded joint, but the elongation of FBW welded joint is significantly lower than that of CMT. Because no filler metal in FBW WM is used to adjust toughness, small amount of carbides in WM induces the weaker pinning effect, which leads to low
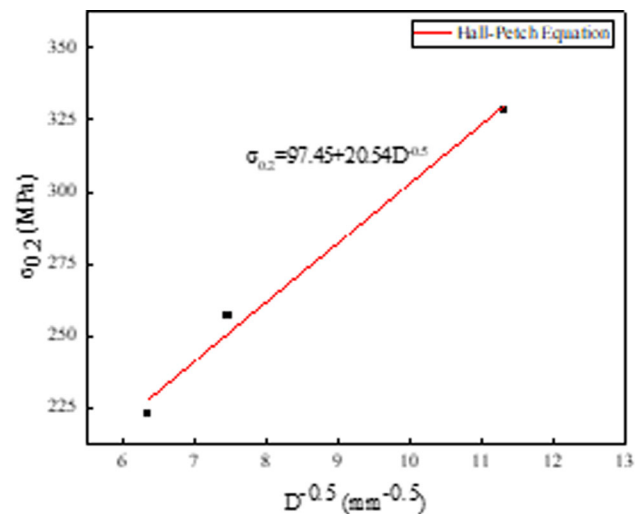

Fig. 14 The relationship between yield strength ($\sigma_{0.2}$) and inverse square root of the average grain size ($D^{-0.5}$)

elongation for FBW welded joint. For TIG welded joint, Fig. 4(b), 5(a) and 7 shows that coarse grains are produced in WM and M390 CGHAZ due to excessive heat input. Figure 6(a) shows that the brittle martensite is produced in TIG WM and M390 CGHAZ. The above two factors lead to poor mechanical properties of TIG welded joint.

4.4 Reason of Corrosion Resistance Difference for Three Welded Joints

The chemical composition, relative proportion of austenite and martensite are the key reasons for the differences in corrosion resistance of the three welded joints.

First of all, the chemical composition of Cr and Ni in the three welded joints has changed. Combined with Fig. 12 and 13, it can be seen that the distribution of Cr element in the FBW welded joint with the worst corrosion resistance is uneven, and the pitting corrosion almost completely occurs in the Cr-poor area and the size is uneven, while the CMT welded joint with the best corrosion resistance has smaller and more uniform pitting pits due to the rich Ni element. This is because higher Cr and higher Ni have stronger corrosion resistance (Ref 54, 55), which were more favorable to protect the passivation film and slowing corrosion. Secondly, the addition of ERNi-1 nickel-based welding wire increases the proportion of austenite phase in the welded joint, resulting in the best corrosion resistance. In the FBW welded joint, the proportion of austenite decreased, whereas the proportion of austenite in the TIG welded joint was the lowest and the proportion of martensite was the highest. In Fig. 6, the phase compositions of the three welded joints are compared, and it can be seen that the phase compositions of the three weld metals have altered dramatically, while the other parts of the welded joints have relatively unchanged. The proportion of austenite in weld metal reduces from CMT to FBW to TIG joints, while the proportion of martensite grows and the martensitic transformation increases, resulting in high lattice distortion and strain levels. Because the martensite microstructure has a low amount of Cr-containing components, pitting corrosion can easily be formed here at high strain levels. Thirdly, different Cr and Ni contents of martensite and austenite make it possible to generate a Cr barren zone at the martensite–austenite interface (Ref 56), which is the most crucial to induce the occurrence of corrosion. This can also explain that part of the pitting corrosion of FBW and TIG welded joints in Fig. 13 occurs on the Cr-poor and Cr-rich interfaces. The CMT weld metal has the smallest phase interface proportion, whereas the FBW weld metal has the most phase interface proportion. The more the phase interface proportion is, the worse the corrosion resistance is. Based on above studies, TIG welded M390 and 304 stainless steel joints can be used in the joining of thin plate joints when there are no more loading requirements. CMT welded M390 and 304 stainless steel joints due to the addition of nickel-based metals as welding wire are widely in used corrosive environments when the requirement of the mechanical properties and corrosion resistance is crucial. The flash butt welded joint can be used in simple structure.

5. Conclusion

The microstructure and properties of M390 high carbon martensitic stainless steel and 304 austenitic stainless steel under three welding methods of TIG, CMT and FBW are compared. Based on the aforementioned results, the main conclusions can be drawn as follows:

(1) Tensile strength of three types of welded joints is lower than that of M390 BM and 304 BM. CMT welded joint has the highest tensile strength and best toughness among three types of welded joints. TIG welded joint has the lowest tensile strength and worst toughness.

(2) The changes of three welded joints' hardness are different. In the TIG welded joint, the difference of the hardness between the heat-affected zone and WM is small. In the CMT welded joint, the difference of the hardness between M390 CGHAZ and WM is large. In an FBW welded joint, from M390 side to 304 side of weld metal, the hardness of the FBW welded joint gradually decreases. The varied hardness trends are mainly attributed to two reasons: First, the matrix microstructures of the three types of WM are different; secondly, the degree of element diffusion in the welded joints has some difference.

(3) Cleavage fracture dominates the fracture surface of TIG welded joint. Ductile fracture dominates the fracture surface of CMT welded joint. Brittle fracture dominates the fracture surfaces of TIG welded joint. The fracture positions of the three welded joints are all in WM, but the reasons for the fracture are not the same.

(4) CMT welded joint has the best corrosion resistance, which is due to the filling of nickel-based alloys in weld metal. FBW welded joint has poor corrosion resistance, because of the uneven chemical composition of the weld and the creation of a high number of martensitic structures and phase interfaces. The corrosion resistance of FBW welded joint can be improved with heat treatment.

Conflict of interest

The authors declare that they have no known competing financial interests or personal relationships that could have appeared to influence the work reported in this paper.

Ethical Approval

This article does not contain any studies with human participants or animals performed by any of the authors.

References

1. M. Sharifitabar and A. Halvaee, Resistance Upset Butt Welding of Austenitic to Martensitic Stainless Steels, *Mater. Des.*, 2010, **31**(6), p 3044–3050.

2. G. Singh, R.K. Saxena and S. Pandey, An Examination of Mechanical Properties of Dissimilar AISI 304 Stainless Steel and Copper Weldment Obtained Using GTAW, *Mater. Today Proc.*, 2020, **26**, p 2783–2789.

3. M. Cheng, P. He, L. Lei, X. Tan, X. Wang, Y. Sun, J. Li and Y. Jiang, Comparative Studies on Microstructure Evolution and Corrosion Resistance of 304 and a Newly Developed High Mn and N Austenitic Stainless Steel Welded Joints, *Corros. Sci.*, 2021, **183**, p 109338.

4. Z. Dang, G. Qin and H. Ma, Interfacial Microstructural Characterization and Mechanical Properties of Inertia Friction Welding of 2219 Aluminum Alloy to 304 Stainless Steel, *Mater. Sci. Eng. A*, 2021, **822**, p 141689.

5. J. Yang, Y. Wang, F. Li, W. Huang, G. Jing, Z. Wang and X. Zeng, Weldability, Microstructure and Mechanical Properties of Laser-welded Selective Laser Melted 304 Stainless Steel Joints, *J. Mater. Sci. Technol.*, 2019, **35**(9), p 1817–1824.

6. A.R. Biswas, S. Chakraborty, P.S. Ghosh and D. Bose, Study of Parametric Effects on Mechanical Properties of Stainless Steel (AISI 304) and Medium Carbon Steel (45C8) Welded Joint Using GMAW, *Mater. Today Proc.*, 2018, **5**(5), p 12384–12393.

7. P.B. Srinivasan, S.W. Sharkawy and W. Dietzel, Environmental Cracking Behavior of Submerged Arc-Welded Supermartensitic Stainless Steel Weldments, *J. Mater. Eng. Perform.*, 2004, **13**(2), p 232–236.

8. M. Erdem, M. Altuğ and M. Karabulut, Investigation of Mechanical, Microstructural, and Machining Properties of AISI 420 Martensitic Stainless Steel Welded by Laser Welding, *Int. J. Adv. Manuf. Technol.*, 2015, **85**(1–4), p 481–492.

9. S.H. Baghjari and S.A.A. AkbariMousavi, Experimental Investigation on Dissimilar Pulsed Nd:YAG Laser Welding of AISI 420 Stainless Steel to Kovar Alloy, *Mater. Des.*, 2014, **57**, p 128–134.

10. M.P. Satish Kumar and P. Bala Srinivasan, Corrosion Behaviour of a Thin Section Martensitic Stainless Steel GTA Weldment in Chloride Solutions, *Mater. Lett.*, 2008, **62**, p 2887–2890.

11. J.R. Berretta, W. de Rossi, M.D. das Neves, I.A. de Almeida and N.D. Vieira Junior, Pulsed Nd:YAG Laser Welding of AISI 304 to AISI 420 Stainless Steels, *Opt. Lasers Eng.*, 2007, **45**(9), p 960–966.

12. K. Kumar, S. Chandra Deheri and M. Masanta, Effect of Activated Flux on TIG Welding of 304 Austenitic Stainless Steel, *Mater. Today Proc.*, 2019, **18**, p 4792–4798.

13. S. Cui, Z. Liu, Y. Fang, Z. Luo, S.M. Manladan and S. Yi, Keyhole Process in K-TIG Welding on 4 mm Thick 304 Stainless Steel, *J. Mater. Process. Technol.*, 2017, **243**, p 217–228.

14. Q. Lixue, Y. Gang, D. Hao, C. Rui, C. Hongyan, W. Tiejun, Effect of Heat Treatment Process on Microstructure and Mechanical Properties of M390/304 CMT Welded Joints, Transactions Of The China Welding Institution

15. M. Pouranvari, Fracture Toughness of Martensitic Stainless Steel Resistance Spot Welds, *Mater. Sci. Eng. A*, 2017, **680**, p 97–107.

16. L. Pan, C.T. Kwok and K.H. Lo, Friction-stir Processing of AISI 440C High-carbon Martensitic Stainless Steel for Improving Hardness and Corrosion Resistance, *J. Mater. Process. Technology*, 2020, **277**, p 116448.

17. C.A. Della Rovere, C.R. Ribeiro, R. Silva, N.G. Alcântara and S.E. Kuri, Local Mechanical Properties of Radial Friction Welded Supermartensitic Stainless Steel Pipes, *Mater. Des. (1980–2015)*, 2014, **56**, p 423–427.

18. A. Ozlati and M. Movahedi, Effect of Welding Heat-input on Tensile Strength and Fracture Location in Upset Resistance Weld of Martensitic Stainless Steel to Duplex Stainless Steel Rods, *J. Manuf. Process.*, 2018, **35**, p 517–525.

19. Q. Zhang, J. Zhang, P. Zhao, Y. Huang, Z. Yu and X. Fang, Low-cycle Fatigue Behaviors of a New Type of 10% Cr Martensitic Steel and Welded Joint with Ni-Based Weld Metal, *Int. J. Fatigue*, 2016, **88**, p 78–87.

20. Z. Sun and T. Moisio, Laser Beam Welding of Austenitic/Ferritic Dissimilar Steel Joints Using Nickel Based Filler Wire, *Mater. Sci. Technol.*, 2013, **9**(7), p 603–608.

21. S. Mahajan and R. Chhibber, Investigations on Dissimilar Welding of P91/SS304L Using Nickel-Based Electrodes, *Mater. Manuf. Processes*, 2020, **35**(9), p 1010–1023.

22. S. Sirohi, C. Pandey and A. Goyal, Role of the Ni-Based Filler (IN625) and Heat-Treatment on the Mechanical Performance of the GTA Welded Dissimilar Joint of P91 and SS304H Steel, *J. Manuf. Process.*, 2021, **65**, p 174–189.

23. P. Sharma and D.K. Dwivedi, Improving the Strength-Ductility Synergy and Impact Toughness of Dissimilar Martensitic-Austenitic Steel Joints by A-TIG Welding with Wire Feed, *Mater. Lett.*, 2021, **285**, p 129063.

24. A. Kulkarni, D.K. Dwivedi and M. Vasudevan, Dissimilar Metal Welding of P91 Steel-AISI 316L SS with Incoloy 800 and Inconel 600 Interlayers by Using Activated TIG Welding Process and its Effect on the Microstructure and Mechanical Properties, *J. Mater. Process. Technol.*, 2019, **274**, p 116280.

25. M. Sabzi, S.H. Mousavi Anijdan, A.R. Eivani, N. Park and H.R. Jafarian, The Effect of Pulse Current Changes in PCGTAW on Microstructural Evolution, Drastic Improvement in Mechanical Properties, and Fracture Mode of Dissimilar Welded Joint of AISI 316L-AISI 310S Stainless Steels, *Mater. Sci. Eng. A*, 2021, **823**, p 141700.

26. M. Sabzi, S.H. Mousavi Anijdan, A.R.B. Chalandar, N. Park, H.R. Jafarian and A.R. Eivani, An Experimental Investigation on the Effect of Gas Tungsten Arc Welding Current Modes upon the Microstructure, Mechanical, and Fractography Properties of Welded Joints of Two Grades of AISI 316L and AISI310S Alloy Metal Sheets, *Mater. Sci. Eng. A*, 2022, **840**, p 142877.

27. M. Sabzi and S.M. Dezfuli, Drastic Improvement in Mechanical Properties and Weldability of 316L Stainless Steel Weld Joints by Using Electromagnetic Vibration During GTAW Process, *J. Manuf. Process.*, 2018, **33**, p 74–85.

28. T. Reza Tabrizi, M. Sabzi, S.H. Mousavi Anijdan, A.R. Eivani, N. Park and H.R. Jafarian, Comparing the Effect of Continuous and Pulsed Current in the GTAW Process of AISI 316L Stainless Steel Welded Joint: Microstructural Evolution, Phase Equilibrium, Mechanical Properties and Fracture Mode, *J. Mater. Res. Technol.*, 2021, **15**, p 199–212.

29. S.H. Mousavi Anijdan, M. Sabzi, M. Ghobeiti-Hasab and A. Roshan-Ghiyas, Optimization of Spot Welding Process Parameters in Dissimilar Joint of Dual Phase Steel DP600 and AISI 304 Stainless Steel to Achieve the Highest Level of Shear-tensile Strength, *Mater. Sci. Eng. A*, 2018, **726**, p 120–125.

30. L. Su, Z. Fei, B. Davis, H. Li and H. Bornstein, Digital Image Correlation Study on Tensile Properties of High Strength Quenched and Tempered Steel Weld Joints Prepared by K-TIG and GMAW, *Mater. Sci. Eng. A*, 2021, **827**, p 142033.

31. N. Saini, C. Pandey, M.M. Mahapatra, H.K. Narang, R.S. Mulik and P. Kumar, A Comparative Study of Ductile-Brittle Transition Behavior and Fractography of P91 and P92 Steel, *Eng. Fail. Anal.*, 2017, **81**, p 245–253.

32. V. Dudko, A. Fedoseeva and R. Kaibyshev, Ductile-Brittle Transition in a 9% Cr Heat-resistant Steel, *Mater. Sci. Eng. A*, 2017, **682**, p 73–84.

33. M.T. Kazemi, H. Golsorkhtabar, M.H.A. Beygi and M. Gholamitabar, Fracture Properties of Steel Fiber Reinforced High Strength Concrete Using Work of Fracture and Size Effect Methods, *Constr. Build. Mater.*, 2017, **142**, p 482–489.

34. X. Yuan, L. Chen, Y. Zhao, H. Di and F. Zhu, Influence of Annealing Temperature on Mechanical Properties and Microstructures of a High Manganese Austenitic Steel, *J. Mater. Process. Technol.*, 2015, **217**, p 278–285.

35. Y. Peng, C. Wu, J. Gan and J. Dong, Determination of the Local Constitutive Properties of the Welded Steel Joints Using Digital Image Correlation Method, *Constr. Build. Mater.*, 2018, **171**, p 485–492.

36. H.R. Jafarian, M. Sabzi, S.H. Mousavi Anijdan, A.R. Eivani and N. Park, The Influence of Austenitization Temperature on Microstructural Developments, Mechanical Properties, Fracture Mode and Wear Mechanism of Hadfield High Manganese Steel, *J. Mater. Res. Technol.*, 2021, **10**, p 819–831.

37. M. Sabzi and S.M. Dezfuli, Post Weld Heat Treatment of Hypereutectoid Hadfield Steel: Characterization and Control of Microstructure, Phase Equilibrium, Mechanical Properties and Fracture Mode of Welding Joint, *J. Manuf. Process.*, 2018, **34**, p 313–328.

38. H.T. Wang, G.Z. Wang, F.Z. Xuan, C.J. Liu and S.T. Tu, Local Mechanical Properties of a Dissimilar Metal Welded Joint in Nuclear Powersystems, *Mater. Sci. Eng. A*, 2013, **568**, p 108–117.

39. Y. Wu, Y. Cai, H. Wang, S. Shi, X. Hua and Y. Wu, Investigation on Microstructure and Properties of Dissimilar Joint Between SA553 and SUS304 made by Laser Welding with Filler Wire, *Mater. Des.*, 2015, **87**, p 567–578.

40. H.T. Wang, G.Z. Wang, F.Z. Xuan and S.T. Tu, Fracture Mechanism of a Dissimilar Metal Welded Joint in Nuclear Power Plant, *Eng. Fail. Anal.*, 2013, **28**, p 134–148.

41. C. Pandey and M.M. Mahapatra, Effect of Groove Design and Post-weld Heat Treatment on Microstructure and Mechanical Properties of P91 Steel Weld, *J. Mater. Eng. Perform.*, 2016, **25**(7), p 2761–2775.

42. M. Abd El-Rahman Abd El-Salam, I. El-Mahallawi and M.R. El-Koussy, Influence of Heat Input and Post-weld Heat Treatment on

Boiler Steel P91 (9Cr-1Mo-V-Nb) Weld Joints Part 2—Mechanical Properties, *Int. Heat Treat. Surf. Eng.*, 2013, **7**(1), p 32–37.

43. S.S. Wang, D.L. Peng, L. Chang and X.D. Hui, Enhanced Mechanical Properties Induced by Refined Heat Treatment for 9Cr–0.5Mo–1.8W Martensitic Heat Resistant Steel, *Mater. Des.*, 2013, **50**, p 174–180.

44. Y.K. Yang, Macrosegregation in arc welds caused by dissimilar filler metals. The University of Wisconsin—Madison (2008)

45. C. Barr, S. Da Sun, M. Easton, N. Orchowski, N. Matthews and M. Brandt, Influence of Macrosegregation on Solidification Cracking in Laser Clad Ultra-high Strength Steels, *Surf. Coat. Technol.*, 2018, **340**, p 126–136.

46. Y. Zhang, M. Hu, Z. Cai, C. Han, X. Li, X. Huo, M. Fan, S. Rui, K. Li and J. Pan, Effect of Nickel-Based Filler Metal Types on Creep Properties of Dissimilar Metal Welds Between Inconel 617B and 10% Cr Martensitic Steel, *J. Market. Res.*, 2021, **14**, p 2289–2301.

47. Y.-Y. You, R.-K. Shiue, R.-H. Shiue and C. Chen, The Study of Carbon Migration in Dissimilar Welding of the Modified 9Cr-1Mo Steel, *J. Mater. Sci. Lett.*, 2001, **20**(15), p 1429–1432.

48. M. Huang, L. Wang, S. Ya et al., Study on Carbon Diffusion in Cr5Mo/ Cr21Ni12 Dissimilar Metal Welds, *Acta Metall. Sin.*, 2000, **36**(9), p 902–906.

49. L. Falat, M. Svoboda, A. Výrostková, I. Petryshynets and M. Sopko, Microstructure and Creep Characteristics of Dissimilar T91/TP316H Martensitic/Austenitic Welded Joint with Ni-Based Weld Metal, *Mater. Charact.*, 2012, **72**, p 15–23.

50. M. Gittos and T. Gooch, The Interface Below Stainless Steel and Nickel-Alloy Claddings, *Carbon*, 1992, **2**, p 4Cr-Cr1.

51. M. Pouranvari, On the Weldability of Grey Cast Iron Using Nickel Based Filler Metal, *Mater. Des.*, 2010, **31**(7), p 3253–3258.

52. M. Velu and S. Bhat, Experimental Investigations of Fracture and Fatigue Crack Growth of Copper-Steel Joints arc Welded Using Nickel-base Filler, *Mater. Des.*, 2015, **67**, p 244–260.

53. M. Balasubramanian, M.V. Choudary, A. Nagaraja et al., Cold Metal Transfer Process–A Review, *Mater. Today Proc.*, 2020, **33**, p 543–549.

54. Z. Lai, P. Bi, L. Wen, Y. Xue and Y. Jin, Local Electrochemical Properties of Fusion Boundary Region in SA508-309L/308L Overlay Welded Joint, *Corros. Sci.*, 2019, **155**, p 75–85.

55. H.-Y. Ha, M.-H. Jang, T.-H. Lee and J. Moon, Interpretation of the Relation Between Ferrite Fraction and Pitting Corrosion Resistance of Commercial 2205 Duplex Stainless Steel, *Corros. Sci.*, 2014, **89**, p 154–162.

56. S. Wang, Q. Ma and Y. Li, Characterization of Microstructure, Mechanical Properties and Corrosion Resistance of Dissimilar Welded Joint Between 2205 Duplex Stainless Steel and 16MnR, *Mater. Des.*, 2011, **32**(2), p 831–837.

57. E. Hall, The Deformation and Ageing of Mild Steel: III discussion of Results, *Proc. Phys. Soc. B*, 1951, **64**(9), p 747–753.

58. N. Petch, The Cleavage Strength of Polycrystals, *J. Iron Steel Inst.*, 1953, **174**, p 25–28.

59. L. Tan, D. Li, L. Yan, X. Pang and K. Gao, Simultaneous Enhancement of Strength-Ductility via Multiple Precipitates and Austenite in a Novel Precipitation-hardened Martensitic Stainless Steel, *Mater. Sci. Eng. A*, 2023, **873**, p 145062.

60. S.-J. Park, K.-S. Kim, J.-H. Kang and S.-J. Kim, Effects of Carbon and Nitrogen on Hall-Petch Relationship in Austenitic Stainless Steel, *J. Market. Res.*, 2022, **19**, p 2960–2964.

61. S.V. Astafurov, G.G. Maier, E.V. Melnikov, V.A. Moskvina, M.Y. Panchenko and E.G. Astafurova, The Strain-Rate Dependence of the Hall-Petch Effect in Two Austenitic Stainless Steels with Different Stacking Fault Energies, *Mater. Sci. Eng. A*, 2019, **756**, p 365–372.